Interannual Variability of the North Pacific Subtropical Countercurrent and Its Associated Mesoscale Eddy Field

BO QIU AND SHUIMING CHEN

Department of Oceanography, University of Hawaii at Manoa, Honolulu, Hawaii

ABSTRACT

Interannual changes in the mesoscale eddy field along the Subtropical Countercurrent (STCC) band of 18°–25°N in the western North Pacific Ocean are investigated with 16 yr of satellite altimeter data. Enhanced eddy activities were observed in 1996–98 and 2003–08, whereas the eddy activities were below average in 1993–95 and 1999–2002. Analysis of repeat hydrographic data along 137°E reveals that the vertical shear between the surface eastward-flowing STCC and the subsurface westward-flowing North Equatorial Current (NEC) was larger in the eddy-rich years than in the eddy-weak years. By adopting a 2½-layer reduced-gravity model, it is shown that the increased eddy kinetic energy level in 1996–98 and 2003–08 is because of enhanced baroclinic instability resulting from the larger vertical shear in the STCC–NEC's background flow. The cause for the STCC–NEC's interannually varying vertical shear can be sought in the forcing by surface Ekman temperature gradient convergence within the STCC band. Rather than El Niño–Southern Oscillation signals as previously hypothesized, interannual changes in this Ekman forcing field, and hence the STCC–NEC's vertical shear, are more related to the *negative* western Pacific index signals.

1. Introduction

Accumulation of high-quality sea surface height (SSH) data from satellite altimeters over the past 16 years has provided us not only a tool to monitor changes in the World Ocean's mesoscale eddy field but also a means to explore the relationship between the time-varying eddy signals and the background mean flow field. In the western North Pacific Ocean, enhanced mesoscale eddy variability is concentrated in two well-defined zonal bands (Fig. 1): one band is along the path of the Kuroshio and its Extension east and southeast of Japan along ~35°N, and the second band is centered along ~22°N east of Taiwan.

The fact that this second enhanced eddy variability band is associated with the North Pacific Subtropical Countercurrent (STCC) has been noted by several recent studies (e.g., Qiu 1999; Roemmich and Gilson 2001; Kobashi and Kawamura 2002; Noh et al. 2007). Figure 2 shows the typical latitude–depth section of time-mean temperature and zonal geostrophic velocity in the western North Pacific Ocean. Embedded in the broad, westward-flowing, wind-driven tropical/subtropical flows between 8° and 30°N, the time-mean STCC appears as a relatively shallow and weak eastward current within the 18°–25°N band. The STCC's existence is geostrophically related to the northward rise of the upper portion of the main thermocline that reverses the westward vertical shear of the wind-driven North Equatorial Current (NEC). The upward-tilting thermocline of the STCC is often referred to as the Subtropical Front.

Theories explaining the generation of the time-mean STCC or Subtropical Front are wide ranging. They include Ekman convergence induced by westerlies to the north and trades to the south (e.g., Roden 1975; Welander 1981), surface buoyancy forcing coupled with geostrophic circulation convergence (Cushman-Roisin 1984; Kubokawa 1997), spontaneous shock in adiabatic wind-driven gyre (Dewar 1992), and intersection of mixed-layer front with outcropping isopycnals (Kubokawa 1999; Kubokawa and Inui 1999). It is important to note that these proposed processes need not to be mutually exclusive. Several processes could be at work in generating the time-mean STCC thermal structures shown in Fig. 2.

Seasonal changes in the STCC and its associated mesoscale eddy field have been examined extensively in the past. Intensity of the STCC has been observed to peak in spring and reach a minimum in fall (e.g., White

Corresponding author address: Dr. Bo Qiu, Department of Oceanography, University of Hawaii at Manoa, 1000 Pope Road, Honolulu, HI 96822.
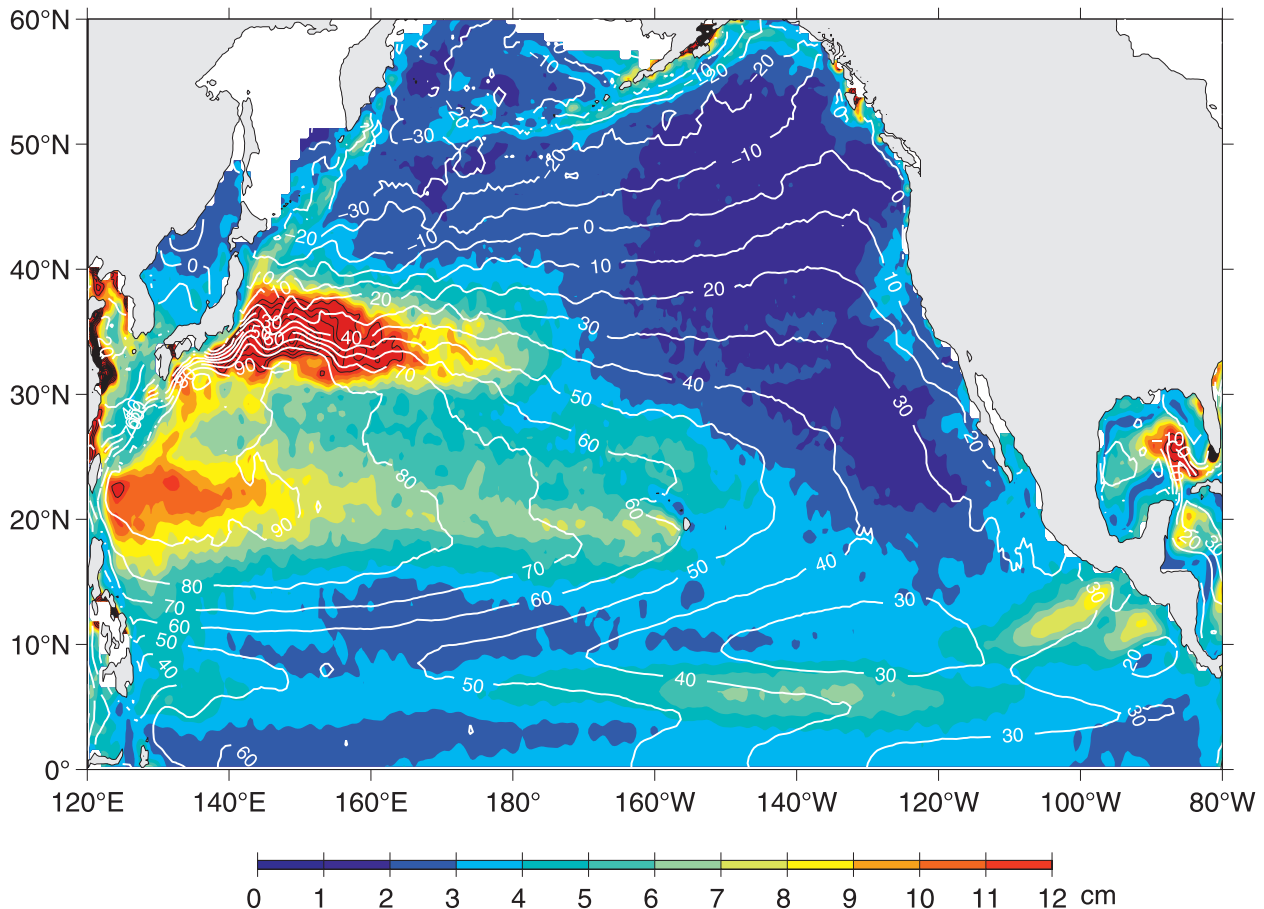E-mail: bo@soest.hawaii.edu

FIG. 1. Root-mean-squared (rms) SSH variability in the North Pacific based on high-pass-filtered satellite altimeter data from October 1992 to April 2009. The high-pass filter has a half-power at 180 days. Regions where the rms SSH variability exceeds 12 cm are indicated by thin black contours (with a contour interval at 2 cm). White contours denote the mean SSH field by Niiler et al. (2003). Unit in cm.

et al. 1978; Kazmin and Rienecker 1996). With the use of an idealized ocean model, Takeuchi (1986) demonstrated that this observed STCC intensity change was largely due to the seasonal surface wind stress forcing; the seasonally varying surface thermal forcing played only a minor role. One consequence of the seasonal STCC variability is that the vertical shear between the eastward-flowing STCC and the subsurface westward-flowing NEC modulates with the seasons, altering the strength of baroclinic instability of the STCC–NEC system. Reflecting this seasonal modulation in instability, the eddy kinetic energy level within the STCC band undergoes a well-defined annual cycle with a maximum in April/May and a minimum in December/January (Qiu 1999; Kobashi and Kawamura 2002).

Compared to the seasonal variability, our knowledge of the interannual changes of the STCC is more limited. One early study addressing this topic is by White et al. (1978), who analyzed expendable bathythermograph (XBT)/mechanical bathythermograph (MBT) and hydro-graphic data in the western North Pacific from 1954 to 1974 finding that the surface velocity shear of STCC was strong in years when the El Niño events occurred: 1957/58, 1963–65, and 1970/71. More recently, Roemmich and Gilson (2001) examined high-resolution XBT data along the Honolulu–Guam–Taiwan repeat transect. They found there existed more mesoscale eddies in 1996–98 than in other years between 1992 and 1999 (see Roemmich and Gilson 2001, their Fig. 4) and, as a result, the eddy-induced poleward heat transport was found to be larger in 1996–98 when compared to the other years.

The present study has three objectives. The first is to describe the interannual variability in the STCC's meso-scale eddy field based on the now available 16-yr satellite altimeter data. A clear interannual modulation with enhanced eddy activity in 1996–98 and 2003–08 and reduced activity in 1993–95 and 1999–2002 is detected. The second objective is to examine the corresponding changes in the background vertically sheared STCC–NEC system. In addition to analyzing the long-term repeat hydrographic
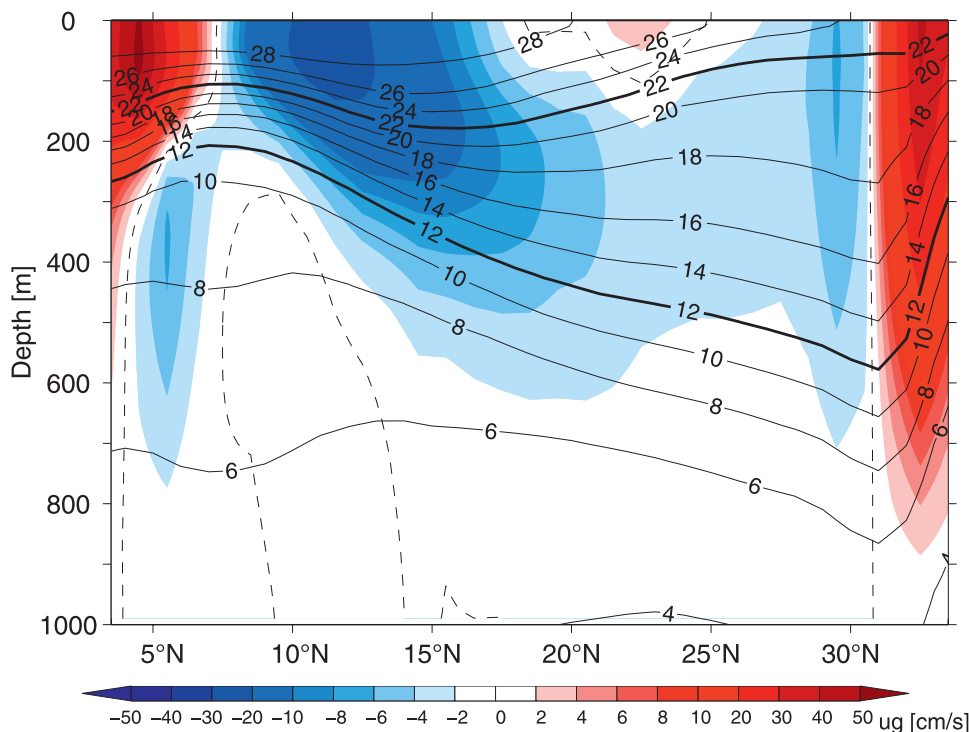
FIG. 2. Latitude–depth section of temperature (solid contours) and zonal geostrophic velocity (color shading) along 137°E from the JMA repeat hydrographic surveys of 1993–2008. The geostrophic velocity is referenced to 1000 dbar and dashed lines denote the zero velocity contours. Notice that the color shading scale is nonlinear.

data along 137°E, we also seek to clarify the cause for the observed STCC–NEC changes in the overlying atmospheric forcing field. Our third objective is to relate the observed interannually varying eddy activities to the stability of the background STCC–NEC system. This is pursued by adopting a 2½-layer reduced-gravity model that mimics the vertically sheared STCC–NEC system.

In Fig. 1, the high eddy variability band along ~22°N appears to extend continuously from east of Taiwan all the way to the Hawaiian Islands. It is important to emphasize that the high eddy variability band west of the Hawaiian Islands that extends to about 180° is centered on 19.5°N and captures the variability associated with the Hawaiian Lee Countercurrent (e.g., Qiu et al. 1997; Xie et al. 2001; Kobashi and Kawamura 2002; Liu et al. 2003). The Hawaiian Lee Countercurrent is formed by dipolar wind stress curl in the lee of the island of Hawaii, and its variability should be considered separately from that of the STCC. In this study, we focus on the eddy variability of the STCC west of the date line.

2. Interannual changes in STCC's eddy variability

To explore the eddy variability along the STCC band, we use in this study the satellite altimetry SSH data compiled by the Collecte Localisation Satellites (CLS) Space Oceanographic Division of Toulouse, France. This dataset merges the TOPEX/Poseidon, *European Remote Sensing Satellite* (*ERS*)-*1/2*, *Geosat Follow-on*, *Jason-1*, and *Jason-2* along-track SSH measurements and provides improved capability for detecting mesoscale SSH signals (Le Traon et al. 1998; Ducet et al. 2000). The dataset has a 7-day temporal resolution, a ⅓°-longitude Mercator spatial resolution, and covers the period from October 1992 through April 2009.

Figure 3a shows the time series of eddy kinetic energy (EKE) averaged in the zonal band of 18°–25°N, 135°–170°E. Here, EKE is calculated from the gridded SSH anomaly data assuming geostrophy. The eastern edge of the band is selected to differentiate the STCC variability from that of the HLCC, and the western edge is chosen to exclude signals of the Kuroshio fluctuations near the western boundary.[1] The time series is dominated by a well-defined annual cycle in which the EKE level is maximum in April/May and minimum in December/January. This EKE annual cycle has been found in

---

[1] Changing the domain of the averaging band does not alter the eddy characteristics discussed in this section.
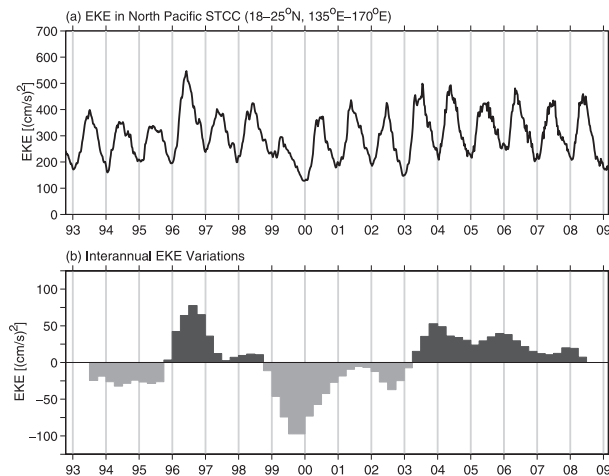
FIG. 3. (a) EKE time series in the North Pacific STCC band of 18°–25°N, 135°–170°E. (b) Interannual changes of the EKE time series after a 1-yr running mean is applied to the original, weekly time series shown in (a); the time series is presented seasonally.

FIG. 4. Variance-preserved power spectra of SSH anomalies as a function of frequency in the STCC region of 18°–25°N, 135°–170°E. Results from the eddy-rich and eddy-weak years are denoted by the solid and dashed lines, respectively.

previous studies to reflect the strength of baroclinic instability of the seasonally modulating vertically sheared STCC–NEC system (Qiu 1999; Kobashi and Kawamura 2002).

In addition to its seasonal modulations, it is also obvious in Fig. 3a that the STCC's EKE field also undergoes changes on interannual time scales. Figure 3b shows the EKE time series after removing the annual running-mean EKE value. As found in the original time series in Fig. 3a, relatively higher EKE levels are detected in 1996–98 and 2003–08, whereas the amplitude of the EKE level is low in other years. Notice that the peak-to-peak amplitude changes for the EKE's annual cycle are about 200~300 cm^2 s^{-2}; in comparison, the peak-to-peak interannual EKE changes have about half that amplitude. Despite this smaller amplitude, the interannual EKE changes nevertheless reach a substantial fraction of the STCC's mean EKE level of ~300 cm^2 s^{-2}. In the following analysis, we will refer to years 1993–95 and 1999–2002, and 1996–98 and 2003–08 as the "eddy weak" and "eddy rich" years, respectively.

To compare how the eddy characteristics differ in the eddy-weak versus eddy-rich years, we present in Fig. 4 the variance-preserved spectra for the SSH anomalies in the STCC band as a function of wave frequency. Compared with the eddy-rich years, the STCC eddies tend to have a more narrow-banded time scale at ~100 days during the eddy-weak years. It is interesting to note that the SSH anomalies have larger variance in the eddy-rich years in *all* frequency bands. In both the eddy-rich and eddy-weak years, the westward-propagating speed of eddies remains nearly constant at 0.092 m s^{-1}. With the dominant eddy time scale at ~100 days, this implies that
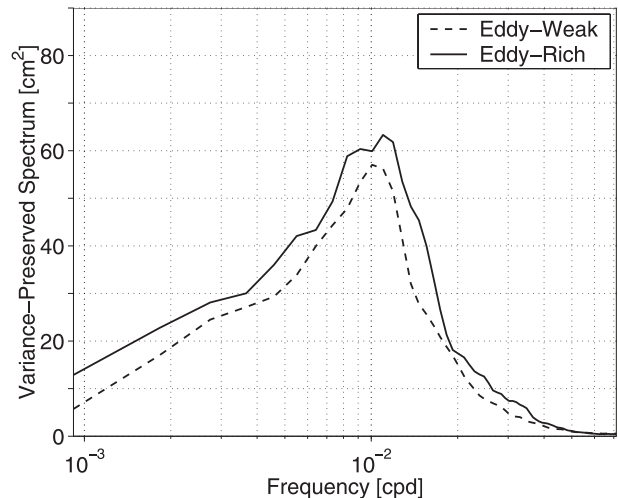
the dominant eddy wavelength along the STCC band is around 800 km throughout the past 16 years. For comparison, the first baroclinic Rossby radius of deformation in the region is ~70 km (Chelton et al. 1998, their Fig. 6).

3. Vertical eddy structures from profiling float measurements

Although the altimetrically derived SSH anomaly data are effective in identifying the seasonal and interannual eddy modulations in the STCC band, it is equally important to examine the *vertical* structure of the eddy signals because it can provide information about their forcing mechanisms. To do so, we use observations from an Argo profiling float that was deployed in the STCC band in late 2004 and remained largely stationary in the area near 22°N, 135°E (see Fig. 5a). The float had the World Meteorological Organization (WMO) identification number 2900432 and measured temperature–salinity (T–S) profiles every 10 days between the surface and its parking depth of 2000 dbar. To put the float-derived T–S data in the context of the altimeter-derived SSH anomaly data, we superimpose in Fig. 5b the available T–S positions/times onto the time–longitude plot of the high-pass-filtered SSH anomalies along 22°N. Although its advection at the parking depth by the NEC is westward, the float tended to drift *eastward* at the surface following the eastward-flowing STCC. The resultant stability in position enables the float to capture the procession of the westward-propagating mesoscale eddy signals along the STCC band as a "moored" profiler.
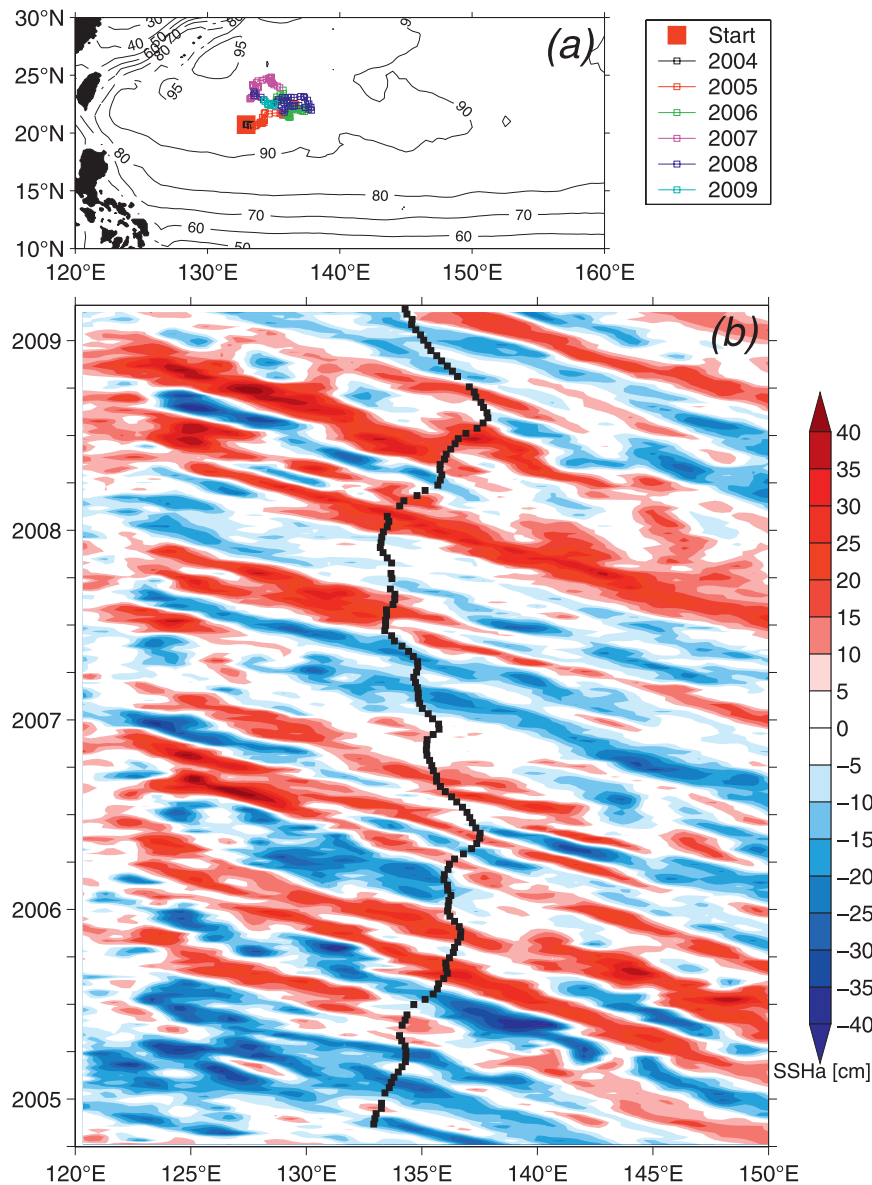
FIG. 5. (a) Trajectories of Argo profiling float 2900432. Contours are the mean SSH field from Niiler et al. (2003) with unit in cm. (b) Time–longitude plot of high-pass-filtered SSH anomalies along 22°N in the western North Pacific from October 2004 to February 2009. Squared marks denote where T–S measurements are made by the Argo profiling float.

Figure 6a compares the collocated SSH anomaly signals derived from the merged altimeter data with those calculated dynamically from the float T–S data. Here, the dynamic calculation has a reference level at 1500 dbar. The comparison is overall very favorable: the linear correlation coefficient (r) between the two time series is 0.92, indicating the mesoscale eddy signals detected by satellite altimeters are adequately captured by the profiling float measurements as well. Figure 6b shows the time series of vertical temperature distributions based on the float's temperature measurements. Although the

time-varying temperature variability is difficult to detect from Fig. 6b, the signals associated with the mesoscale SSH variations become easily discernible when a high-pass filter with a 180-day cutoff period is applied to the original time series (see Fig. 6c). Figure 6c reveals that the temperature anomalies associated with the STCC's mesoscale eddy variability are nearly vertically coherent and extend as deep as 1000 m. In the vertical, the temperature variance has two local maxima centered at the 100- and 420-m depths, which along 22°N correspond to the tilting thermocline associated with the STCC and
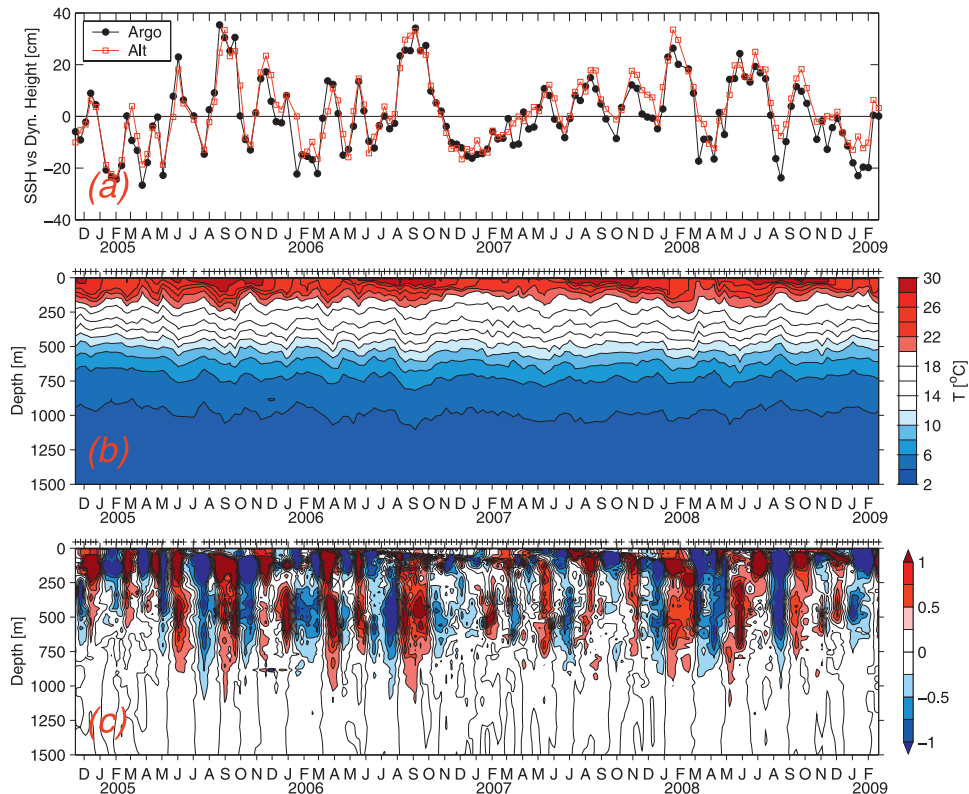
FIG. 6. (a) Time series of the surface dynamic height anomalies (0/1500 dbar) calculated from the profiling float T–S data vs the SSH anomalies measured by satellite altimeters. (b) Vertical temperature profiles derived from the Argo float 2900432; see Fig. 5 for its longitudinal positions and times. (c) Temperature anomaly profiles after a high-pass filter with a 180-day cutoff period is applied to the time series shown in (b).

NEC, respectively (Fig. 2). In the thermostad layer between these two thermoclines (150~350 m), the observed temperature anomalies, as is evident in Fig. 6c, are relatively weak.

To clarify the vertical phase structures of the observed mesoscale eddies, we shift in time the float profiles plotted in Fig. 5b to the fixed longitude 135°E, assuming a westward-translating speed of 0.092 m s^{-1}. For example, the first profile of 13 November 2004 at 132.7°E is shifted to 14 October 2004 after the time-axis transformation. Once the temperature anomaly time series $T'(z, t)$ at the fixed location of 135°E is obtained, we calculate lagged correlations between the $T'(z, t)$ time series at $z = 100$ m and at all other depths. Figure 7 shows the lagged correlation values as a function of depth, where positive lags indicate the lead by the temperature anomalies at the 100-m depth. Notice that with the mesoscale eddies propagating westward, a positive (negative) time lag in Fig. 7 is equivalent to a positive (negative) longitudinal lag in space. Temporally, the oscillatory correlation pattern seen in Fig. 7 indicates that the observed mesoscale eddies have a dominant

wave period at ~100 days, which is consistent with the power spectral analysis result presented in Fig. 4. Vertically, the center of the temperature anomalies exhibits an eastward phase tilt with *increasing* depth. This phase tilt is against the vertical shear of the STCC–NEC system, which tilts eastward with *decreasing* depth (recall Fig. 2). Dynamically, this implies that the observed mesoscale eddies are able to grow at the expense of the vertically sheared STCC–NEC system, or that the background STCC–NEC system is *baroclinically* unstable. This finding from the Argo profiling float data analysis is consistent with the analysis result by Roemmich and Gilson (2001) based on high-resolution XBT data along the Hawaii–Guam–Taiwan repeat transect.

4. Interannual changes in the STCC–NEC mean flow field

To understand the cause underlying the interannual modulations in the STCC's EKE field, it is of interest to look at how the mean flow field of the STCC–NEC system varied over the past 16 years. One unique dataset
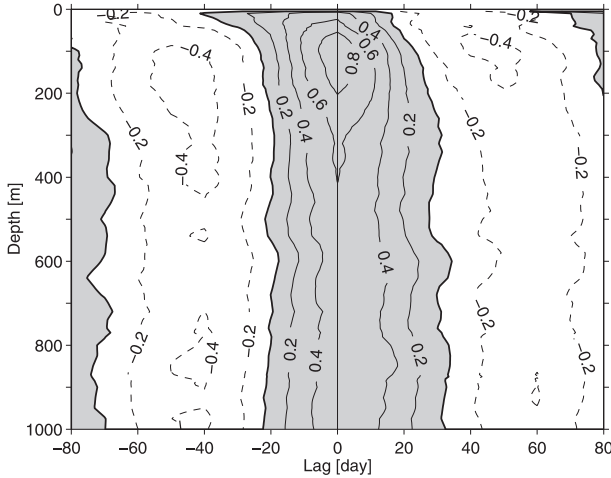
FIG. 7. Lagged correlation coefficients between the temperature anomalies at 100 m and those at other depths. The temperature anomaly time series (before the time-axis adjustment) is shown in Fig. 6c. A positive lag here denotes the lead by the 100-m-depth temperature anomalies. With the number of degrees of freedom estimated at 24 in Fig. 6c, the correlation is significant at the 95% confidence level when $r > 0.404$.

that captures the interannual variations of the STCC–NEC system comes from the repeat hydrographic surveys conducted by the Japan Meteorological Agency (JMA) along the 137°E meridian. The repeat surveys traverse from the coast of Japan at 34°N to offshore of New Guinea at 3°N and, in the STCC–NEC region of our interest, the hydrographic casts have a nominal 1° latitude spatial resolution. Since 1992, JMA has carried out four repeat surveys per year, and the seasonal hydrographic data from 1993 to 2008 are used in our analyses.

Figure 8 compares the latitude–depth sections of temperature and geostrophic zonal flow derived from the repeat hydrographic data in the eddy-weak versus eddy-rich years. Like Fig. 2, the reference level for the geostrophic calculation is set at 1000 dbar. Within the 18°–25°N band, the eastward-flowing STCC in the surface layer is laterally more coherent and has a greater surface velocity in the eddy-rich years than in the eddy-weak years. This difference becomes clearer in Fig. 9 where the zonal geostrophic velocity profiles averaged in 18°–25°N from the contrasting years are superimposed: the surface STCC velocity is ~2 cm s^{-1} in the eddy-rich years, 4 times as large as the surface STCC velocity in the eddy-weak years. Notice that this difference in the surface STCC velocity could have been underestimated, because the STCC's strength in the eddy-rich years is likely weakened by the presence of additional mesoscale eddies. Compared to the surface STCC, changes in the subsurface NEC are more modest between the eddy-

rich and eddy-weak years. At the core depth of the NEC, the zonal velocity difference is ~0.4 cm s^{-1}, which is about 10% of the amplitude of the mean NEC velocity.

With the relatively small STCC difference between the eddy-rich and eddy-weak years, it is important to verify that this difference is statistically significant. To do so, we first form the yearly mean surface STCC velocity time series from the seasonal hydrographic data. By adopting the bootstrap method (Press et al. 1992), we generate 1000 time series by randomizing the order of the observed velocity time series. Applying the composite analysis to these randomized velocity time series reveals that the surface STCC velocity difference shown in Fig. 9 exceeds the 96% significance level over the null hypothesis—namely, there is no difference in the surface STCC velocity between the eddy-rich versus eddy-weak years.

Given that the observed mean flow changes in the STCC–NEC band between the eddy-rich and eddy-weak years are largely confined to the surface 150-m layer, it makes sense to seek the cause for these changes in the regional atmospheric forcing field. Because the vertical shear in the zonal geostrophic velocity (U_g) is related to the meridional temperature (T) gradient through the thermal wind balance:

$$f \frac{\partial U_g}{\partial z} = -\alpha g \frac{\partial T}{\partial y}, \tag{1}$$

where f is the Coriolis parameter, g is the gravity constant, and α is the thermal expansion coefficient, investigating the interannual changes in the surface STCC becomes equivalent to examining the regional meridional temperature gradient changes in the surface 150-m layer. For brevity, we follow Nakamura and Kazmin (2003) and use $G \equiv -\partial T/\partial y$ in place of the meridional temperature gradient. Thus defined, a positive G value indicates an enhanced surface thermocline tilt, or equivalently, a strengthened STCC.

With the STCC existing in the region between the midlatitude westerlies and low-latitude trade winds, an important process that contributes to the interannual changes in G along the STCC band is the Ekman convergence forcing (e.g., Roden 1975; Kazmin and Rienecker 1996). Mathematically, this process can be expressed by

$$\frac{\partial G}{\partial t} \simeq -\frac{\partial}{\partial y} (v_{Ek} G), \tag{2}$$

where $v_{Ek} = -\tau^x/\rho_o f H_o$ is the meridional Ekman velocity averaged in the surface layer, τ^x is the zonal wind stress, ρ_o is the reference density, and H_o (=150 m) is
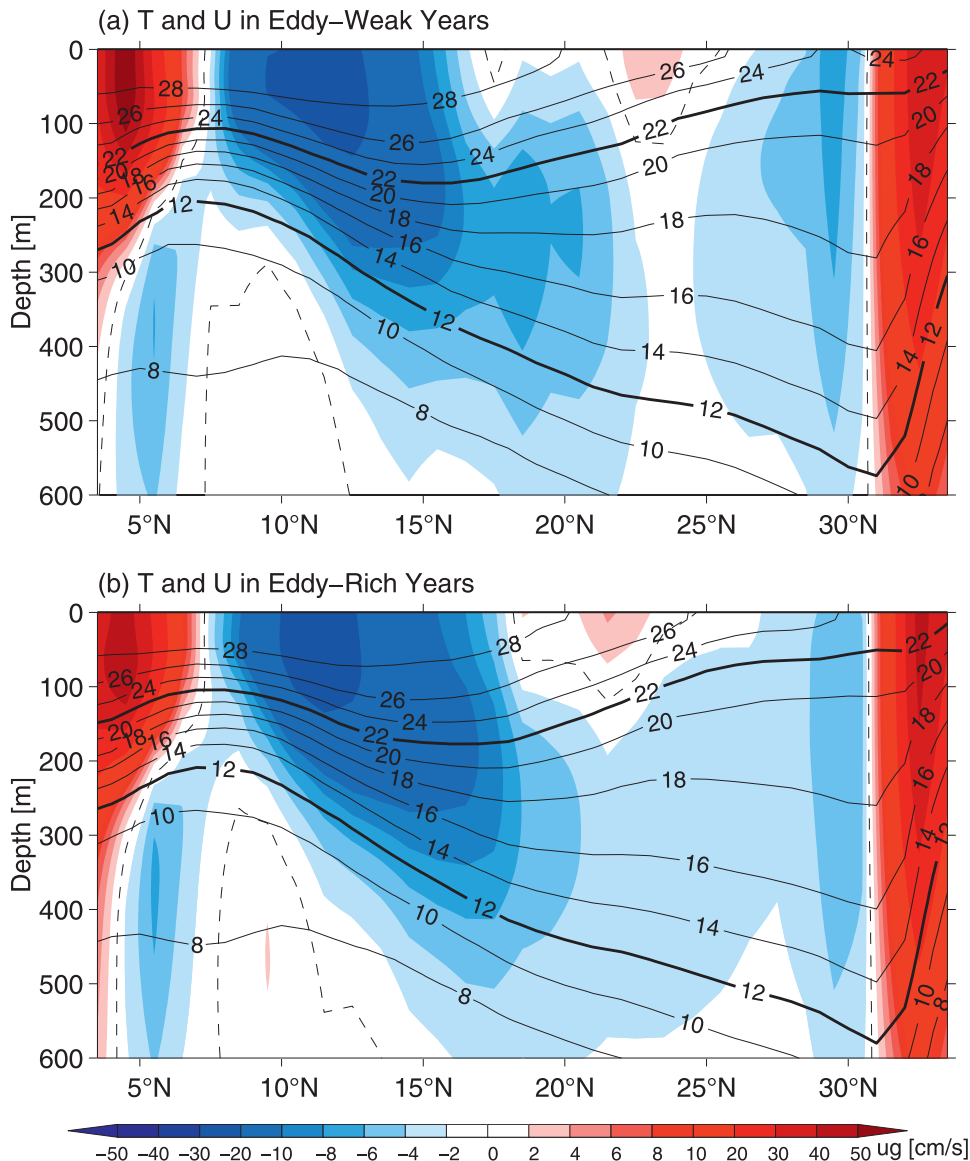
FIG. 8. (a) Latitude–depth section of temperature (solid contours) and zonal geostrophic velocity (colored shading) along 137°E from the JMA repeat hydrographic surveys during the STCC's eddy-weak years of 1993–95 and 1999–2002. The geostrophic velocity is referenced to 1000 dbar and dashed lines denote the zero velocity contours. (b) Same as (a) except for during the STCC's eddy-rich years of 1996–98 and 2003–08.

the thickness of the surface layer. To quantify the rhs of Eq. (2), we use the monthly τ^x data from the National Centers for Environmental Prediction–National Center for Atmospheric Research (NCEP–NCAR) reanalysis (Kistler et al. 2001) and the monthly sea surface temperature data compiled by Reynolds et al. (2002). The Reynolds SST dataset, which combines in situ and satellite temperature measurements, has a 1° horizontal resolution and is adequate in resolving the temperature gradient in the surface STCC layer. Averaged over 1993–2008 and in the band of 18°–25°N, 135°–170°E,

the $-\partial(\upsilon_{Ek}G)/\partial y$ term has a positive value 1.77×10^{-14} °C m^{-1} s^{-1}, indicating that this Ekman forcing term works to maintain the thermocline tilt of STCC against other frontolysis processes.

Figure 10a shows the time series of the interannual $-\partial(\upsilon_{Ek}G)/\partial y$ signals after removal of the annual running-mean value. The time series exhibits modulations similar to the STCC's interannually varying EKE time series derived from the satellite altimeter data (the shaded time series in Fig. 10a). Visually, the time-varying Ekman forcing term appears to lead the EKE time series. This
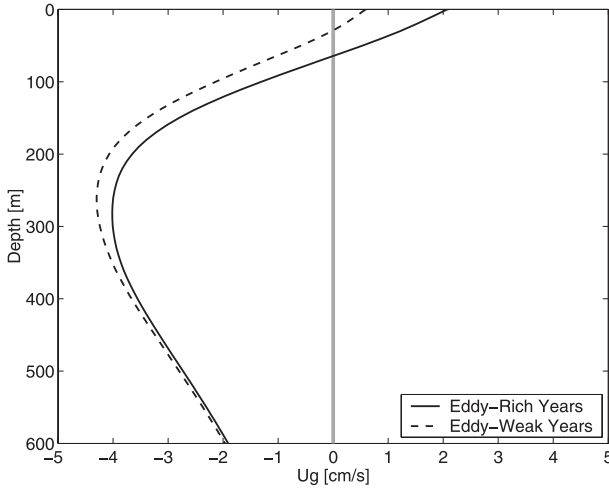
FIG. 9. Zonal geostrophic velocity profiles averaged in the 18°–25°N band along 137°E in the eddy-rich vs eddy-weak years. See Fig. 8 for the detailed latitude–depth sections of the zonal geostrophic velocities.

FIG. 10. (a) Comparison between the interannually-varying Ekman forcing term $-\partial(v_{Ek}G)/\partial y$ (solid line) and the interannually varying EKE time series in the STCC band (shaded bars). The EKE time series is same as that shown in Fig. 3b. (b) Time series of interannually varying Ekman transport convergence $-\partial v_{Ek}/\partial y$.

lead is confirmed in Fig. 11, which indicates that the maximum correlation between the two time series is obtained when the Ekman forcing term leads the EKE time series by ~9 months.[2] The vertically sheared STCC–NEC system, as we will quantify in the next section, is subject to baroclinic instability. Because the vertical shear of the mean flow is weak in the STCC–NEC system, the growth of instability is comparatively slow. The 9-month lead detected in Fig. 11 represents the time required for the STCC–NEC shear to adjust to the time-varying Ekman forcing plus the time for instability of the adjusted STCC–NEC system to fully grow.

Notice that both the Ekman velocity and meridional surface temperature gradient variations can possibly contribute to the $-\partial(v_{Ek}G)/\partial y$ signals presented in Fig. 10a. A look into the v_{Ek} and G fields reveals that much of the interannual variability of $-\partial(v_{Ek}G)/\partial y$ stems from the interannually varying $-\partial v_{Ek}/\partial y$ signals (see Fig. 10b). Physically, this implies that it is the convergence of the time-varying Ekman transport of the time-mean temperature gradient that is responsible for modulating the surface thermocline slope (or, equivalently, the vertical shear) of the STCC–NEC system. This result with regard to the importance of $-\partial(v_{Ek}G)/\partial y$ for the *interannually varying* STCC's strength is in accordance with the previous findings by Takeuchi (1986), who showed that it is the seasonal variations in wind stress, rather
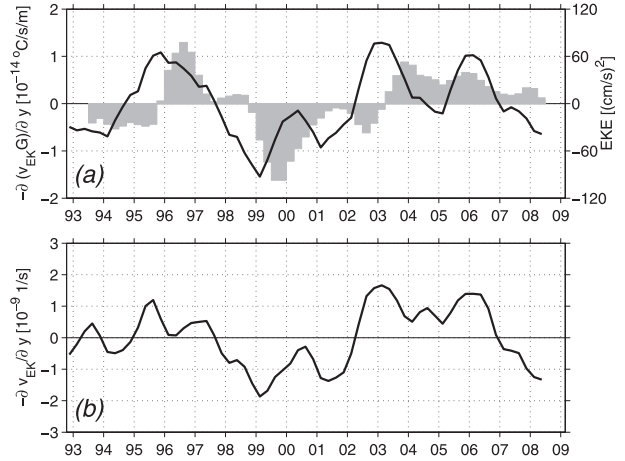
than the surface thermal condition, that determine the *seasonally varying* STCC's strength.

Lastly, it is of interest to verify that the interannually varying $-\partial(v_{Ek}G)/\partial y$ signals shown in Fig. 10a are consistent in magnitude with the STCC changes observed by the in situ hydrographic surveys (i.e., Fig. 9). By combining Eqs. (1) and (2), we have

$$\frac{\partial}{\partial t}\left(\frac{\partial U_g}{\partial z}\right) \simeq -\frac{\alpha g}{f}\frac{\partial}{\partial y}(v_{Ek}G). \qquad (3)$$
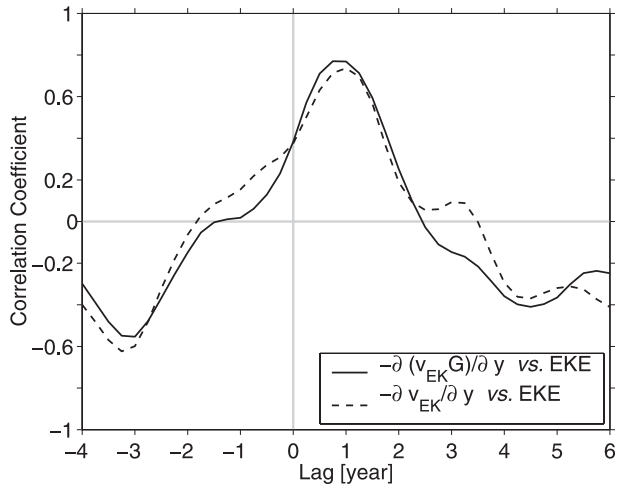

FIG. 11. Solid line: lagged correlation between the interannually varying Ekman forcing term and the EKE time series in the STCC band. See Fig. 10a for the two time series. Dashed line: lagged correlation between the interannually varying Ekman transport convergence term and the EKE time series in the STCC band. A positive lag denotes the lag by the EKE time series.

---

[2] With each year providing an independent sample (i.e., the number of degrees of freedom at 16), the correlation coefficient in Fig. 11 becomes significant at the 95% confidence level when $r > 0.477$.

Assuming most of the interannual changes in U_g are confined to the surface STCC layer (recall Fig. 9), we can estimate the magnitude of the interannual STCC changes by

$$\Delta U_g \simeq \frac{\alpha g H_o}{f} \Delta T \left| \frac{\partial}{\partial y}(v_{\mathrm{Ek}} G) \right|,$$

where ΔT is the wave period of the interannually varying $-\partial (v_{\mathrm{Ek}} G)/\partial y$ signals. From Fig. 10a, $|\partial (v_{\mathrm{Ek}} G)/\partial y|$ is of $O(1 \times 10^{-14}\,°\mathrm{C\,s^{-1}\,m^{-1}})$. Using $\alpha = 2.6 \times 10^{-4}\,°\mathrm{C^{-1}}$, $g = 9.8\,\mathrm{m\,s^{-2}}$, $H_o = 150\,\mathrm{m}$, $\Delta T = 6$ years, and $f = 5.33 \times 10^{-5}\,\mathrm{s^{-1}}$, we have $\Delta U_g \simeq 1.3\,\mathrm{cm\,s^{-1}}$. This estimated ΔU_g value agrees favorably with the observed STCC changes shown in Fig. 9.

5. Stability analysis for interannually varying STCC–NEC system

To explore how the interannual changes in the STCC–NEC system described in the previous section affect the mesoscale eddy field, we follow Qiu (1999) and examine the stability of the vertically sheared STCC–NEC system in a 2½-layer reduced-gravity model. Under the quasigeostrophic approximation, the linearized equations governing the perturbation potential vorticity q_n ($n = 1$ and 2) are

$$\left(\frac{\partial}{\partial t} + U_n \frac{\partial}{\partial x} \right) q_n + \frac{\partial \Pi_n}{\partial y} \frac{\partial \phi_n}{\partial x} = 0, \qquad (4)$$

where ϕ_n is the perturbation streamfunction, U_n is the zonal mean velocity, and Π_n is the mean potential vorticity in layer n (e.g., Pedlosky 1987). Assuming $U_n = $ const, q_n and the meridional gradient of Π_n are related to the other model variables as follows:

$$q_n = \nabla^2 \phi_n + \frac{(-1)^n}{\lambda_n^2}(\phi_1 - \phi_2 - \gamma_n \phi_2) \quad \text{and} \quad (5)$$

$$\Pi_{ny} = \beta - \frac{(-1)^n}{\lambda_n^2}(U_1 - U_2 - \gamma_n U_2), \qquad (6)$$

where

$$\gamma_n = \frac{\rho_n - \rho_1}{\rho_3 - \rho_2} \quad \text{and} \quad \lambda_n^2 = \frac{(\rho_2 - \rho_1)g H_n}{\rho_o f_o^2}. \qquad (7)$$

In the above equations, ∇^2 denotes the horizontal Laplacian operator, H_n is the mean thickness of layer n, ρ_n is the density of layer n, β is the meridional gradient of the Coriolis parameter, and f_o is the Coriolis parameter at the reference latitude. Defined as in Eq. (7), γ_2 is the

stratification ratio and λ_n gives the internal Rossby radiu of deformation in layer n. The stability of this 2½-layer STCC–NEC system can be analyzed by seeking the normal mode solution: $\phi_n = \mathrm{Re}[A_n \exp i(kx + ly - kct)]$. Substituting ϕ_n into Eq. (4) and requiring nontrivial solutions for A_n leads to a quadratic equation for the complex phase speed $c = c_r + ic_i$ [see Eq. (11) in Qiu 1999].

The observed temperature profiles shown in Fig. 8 indicate there was little change in vertical stratification in the 18°–25°N band between the eddy-rich and eddy-weak years. Given this, we set the following parameters at the fixed values for stability analysis: $\rho_1 = 23.4\sigma_\theta$, $\rho_2 = 26.0\sigma_\theta$, $\rho_3 = 27.75\sigma_\theta$, $H_1 = 150$ m, $H_2 = 300$ m, $f_o = 5.33 \times 10^{-5}$ s^{-1}, and $\beta = 2.12 \times 10^{-11}$ s^{-1} m^{-1}. One parameter that changed significantly between the eddy-rich and eddy-weak years is U_1, the surface layer velocity of STCC. Specifically, Fig. 9 suggests that there is a fourfold change in U_1 between the years with the contrasting EKE levels. Changes in the subsurface NEC velocity U_2 appear, in contrast, more modest. As we noted in section 4, however, the mean flow values plotted in Fig. 9 could be underestimated because of the existence of mesoscale eddies. To circumvent this uncertainty, we will consider U_1 and U_2 in the following analysis as adjustable parameters.

Figure 12a shows the growth rate kc_i as a function of the zonal wavenumber k and U_1. In this calculation, U_2 is fixed at -4.0 cm s^{-1} and l at zero. As U_1 increases in amplitude, both the window for permissible unstable waves widens and the growth rate of instability amplifies. Typical values for the e-folding time scale are $30 \sim 50$ days when $U_1 = 2 \sim 4$ cm s^{-1}. In addition, the most unstable waves tend to shift to a smaller wavenumber (or a longer zonal wavelength) as U_1 increases. Notice that the 2½-layer STCC–NEC system would still be unstable even if U_1 decreases to zero. This is because the U_2 amplitude in this case is sufficiently large, resulting in the potential vorticity gradients in the two layers to reserve signs (i.e., $\Pi_{1y}\Pi_{2y} < 0$).

Figure 12b shows the growth rate as a function of k and U_2 when U_1 is fixed at 2 cm s^{-1}. As U_2 increases in amplitude (i.e., when the NEC moves westward at a greater speed), the enhanced vertical shear again broadens the window for permissible unstable waves and increases the growth rate. Unlike the amplitude of U_1, however, change in the U_2 amplitude has little effect upon the preferred wavelength of the most unstable waves. As the amplitude of U_2 decreases, there exists a threshold value below which the 2½-layer STCC–NEC system becomes stable. Dynamically, it is possible to prove that the necessary and *sufficient* condition for instability in the present 2½-layer model is that the minimum shear between STCC and NEC exceeds
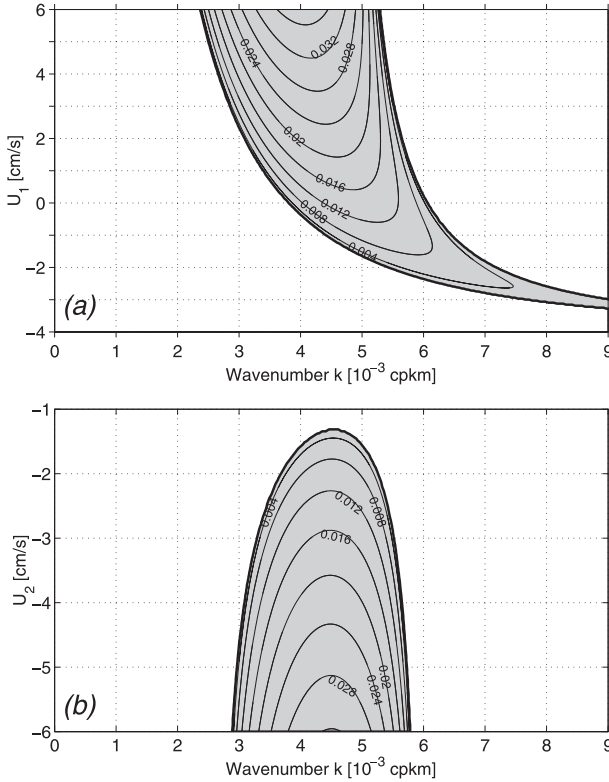
FIG. 12. Growth rate dependence on (a) U_1 and (b) U_2 in the 2½-layer STCC–NEC model. In (a) and (b), U_2 and U_1 are fixed at −0.4 and 2.0 cm s^{-1}, respectively. Shaded areas denote the baroclinically unstable domain. Contour units are day^{-1}.

$$(U_1 - U_2)_{\min} > \lambda_2^2 \beta + \gamma_2 U_2 \qquad (8)$$

(see Qiu and Chen 2004). For the parameter values chosen for Fig. 12b, occurrence of instability based on (8) requires $U_2 < (U_1 - \lambda_2^2 \beta)/(1 + \gamma_2) = -1.33$ cm s^{-1}. Thus, threshold U_2 value increases to −2.14 cm s^{-1} when U_1 is reduced to zero. In the case of the NEC in the 18°–25°N band of the western North Pacific Ocean, its velocity amplitude never falls below these threshold values, so the instability condition (8) is *always* satisfied. Although it is always unstable, the magnitude of the instability is sensitive to the background vertical shear between the surface STCC and subsurface NEC. When the surface STCC is strengthened because of the convergent Ekman temperature flux forcing, the enhanced baroclinic instability of the STCC–NEC system likely results in the increased EKE level in the 18°–25°N band, as observed in 1996–98 and 2003–08 (Fig. 3b).

6. Summary and discussion

Satellite altimeter data of the past 16 years are used in this study to investigate the interannual variability in the mesoscale eddy field along the Subtropical Countercurrent band (18°–25°N) in the western North Pacific Ocean. Enhanced eddy activities were observed in 1996–99 and 2003–08, whereas below-average eddy activities were detected in 1993–95 and 2000–02. The interannual eddy kinetic energy modulations have a peak-to-peak amplitude of ~150 cm^2 s^{-2}, corresponding to 50% of the local mean EKE level. The dominant eddy signals in the STCC band have a time scale of ~100 days and a length scale of ~800 km. An examination of their vertical structures based on Argo profiling float measurements reveals that the temperature anomalies of the eddy signals can reach as deep as 1000 dbar and have a vertical phase tilting upward to the west. This phase tilt is against the vertical shear of the STCC and the NEC, indicating that baroclinic instability of the vertically sheared STCC–NEC mean flow is the energy source for the regional enhanced eddy signals along the 18°–25°N band.

By analyzing the JMA repeat hydrographic data along the 137°E meridian, we found the vertical shear between the STCC and NEC was larger in the eddy-rich years than in the eddy-weak years. This is despite the fact that enhanced eddy activity in the eddy-rich years is likely to have weakened the eastward mean flow of the STCC. By simplifying the vertically sheared STCC–NEC system to a 2½-layer reduced-gravity system, we found that the observed STCC–NEC system is subject to baroclinic instability irrespective of the years with differing STCC intensities. That the observed EKE level was high in 1996–98 and 2003–08 was because of the more intense baroclinic instability resulting from the larger vertical shear and, hence, greater available potential energy in the STCC–NEC's background flow.

The interannually modulating vertical shear of the STCC–NEC system is largely related to the thermocline tilt in the surface 150-m layer. An examination of available wind stress and sea surface temperature data reveals that the forcing by Ekman temperature gradient convergence in the STCC band matches well with the interannually varying EKE signals with a lead of approximately nine months. Among the variables contributing to the Ekman forcing term $-\partial(v_{\mathrm{Ek}} G)/\partial y$, it is the Ekman transport convergence signals $-\partial v_{\mathrm{Ek}}/\partial y$ that dictate the term's interannual variations. By analyzing available MBT/XBT and hydrographic data in the western North Pacific Ocean from 1954 to 1974, White et al. (1978) found that the surface Front associated with the STCC (a.k.a. the Subtropical Front) was more intense than average in 1957/58, 1963–65, and 1970/71. They attributed these interannual STCC changes to be connected to the El Niño–Southern Oscillation (ENSO) variability in the tropics.

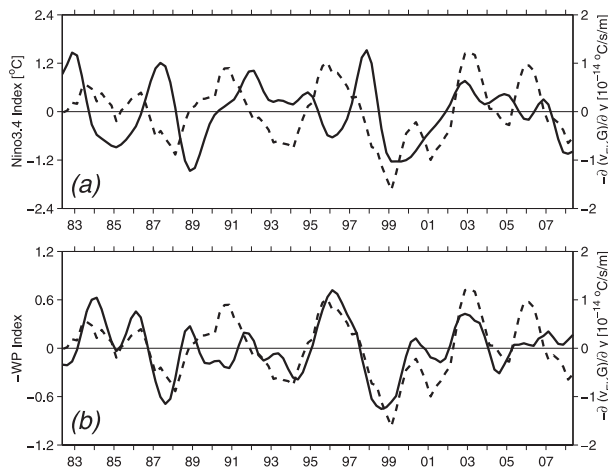To clarify the validity of this connection during the recent decades, we extend the Ekman forcing time series

FIG. 13. (a) Comparison between the interannually varying Niño-3.4 index (solid line) and the Ekman forcing term $-\partial(v_{Ek}G)/\partial y$ (dashed line). (b) Comparison between the interannually varying *negative* WP index (solid line) and the Ekman forcing term. The Niño-3.4 and WP indices are from online (at http://www.cdc.noaa.gov/data/correlation), and their interannual signals are obtained by removing the annual running-mean values.

back to 1982 when the monthly SST data of Reynolds et al. (2002) becomes available. Figure 13a compares the interannually varying Ekman forcing time series (dashed line) with the interannually varying Niño-3.4 index (solid line). The correspondence between these two time series appears marginal: the linear correlation coefficient is only 0.13. Similar marginal correlations are obtained when other indices representing ENSO signals are adopted (e.g., the Southern Oscillation index). The Ekman forcing time series, on the other hand, corresponds well with the interannually varying *negative* western Pacific (WP) index. The linear correlation coeffecient between those two time series shown in Fig. 13b reaches 0.62. As described in Wallace and Gutzler (1981), the western Pacific pattern is a primary mode of the low-frequency atmospheric variability characterized by a north–south dipole of sea level pressure anomalies over the western North Pacific Ocean. The southern center of this pattern is located at 25°N, 165°E over the STCC band of our interest. During the negative phase of the WP index, sea level pressure around the southern center of the WP pattern increases, resulting in increased Ekman transport convergence along the STCC band. Because the Ekman forcing term on interannual time scales is controlled largely by the Ekman transport convergence, a negative WP index would thus lead to an enhanced thermocline tilt of the STCC, as depicted in Fig. 13b. Based on the results of Fig. 13, we conclude that the negative WP index serves as a better indicator for the interannually varying STCC and its associated mesoscale eddy field than an ENSO index.

With the STCC bordered to the north by the subtropical and central mode waters in the western North Pacific (e.g., Kubokawa and Inui 1999; Kobashi et al. 2006), it is natural to ask whether the STCC variability can be induced by changes originating in the mode waters. A recent numerical modeling study by Yamanaka et al. (2008) found that the intensity of their model-simulated STCC was strong in the late 1970s and weak in the early 1990s. They suggested that this decadal STCC change was caused by mode waters, formed under different atmospheric conditions in the midlatitude North Pacific in the 1970s versus the 1990s, being advected southward and modifying the STCC's thermocline tilt. Observationally, this causal relationship is yet to be established. In its formation area southeast of Japan, subtropical mode water variability has been observed to be related to the dynamic state of the Kuroshio Extension (Qiu and Chen 2006). Constrained by the midlatitude North Pacific wind stress curl forcing, the Kuroshio Extension's dynamic state after 1982 has fluctuated with a clear 10-yr period (e.g., Taguchi et al. 2007; Qiu et al. 2007). This 10-yr period does not appear to match the dominantly *interannually varying* STCC signals described in this study. Clearly, more future investigations are needed to clarify how mode water properties modify after their subduction and the extent to which the time-varying mode waters can affect the vertical shear of the STCC–NEC system in comparison with the regional atmospheric forcing along the STCC band.

REFERENCES

Chelton, D. B., R. A. de Szoeke, M. G. Schlax, K. E. Naggar, and N. Siwertz, 1998: Geographical variability of the first baroclinic Rossby radius of deformation. *J. Phys. Oceanogr.,* **28,** 433–460.
Cushman-Roisin, B., 1984: On the maintenance of the Subtropical Front and its associated countercurrent. *J. Phys. Oceanogr.,* **14,** 1179–1190.
Dewar, W. K., 1992: Spontaneous shocks. *J. Phys. Oceanogr.,* **22,** 505–522.

Ducet, N., P. Y. Le Traon, and G. Reverdin, 2000: Global high-resolution mapping of ocean circulation from TOPEX/Poseidon and ERS-1 and -2. *J. Geophys. Res.,* **105,** 19 477–19 498.

Kazmin, A. S., and M. M. Rienecker, 1996: Variability and frontogenesis in the large-scale oceanic frontal zones. *J. Geophys. Res.,* **101,** 907–921.

Kistler, R., and Coauthors, 2001: The NCEP–NCAR 50-Year Reanalysis: Monthly means CD-ROM and documentation. *Bull. Amer. Meteor. Soc.,* **82,** 247–267.

Kobashi, F., and H. Kawamura, 2002: Seasonal variation and instability nature of the North Pacific Subtropical Countercurrent and the Hawaiian Lee Countercurrent. *J. Geophys. Res.,* **107,** 3185, doi:10.1029/2001JC001225.

——, H. Mitsudera, and S.-P. Xie, 2006: Three subtropical fronts in the North Pacific: Observational evidence for mode water-induced subsurface frontogenesis. *J. Geophys. Res.,* **111,** C09033, doi:10.1029/2006JC003479.

Kubokawa, A., 1997: A two-level model of subtropical gyre and subtropical countercurrent. *J. Oceanogr.,* **53,** 231–244.

——, 1999: Ventilated thermocline strongly affected by a deep mixed layer: A theory for subtropical countercurrent. *J. Phys. Oceanogr.,* **29,** 1314–1333.

——, and T. Inui, 1999: Subtropical countercurrent in an idealized ocean GCM. *J. Phys. Oceanogr.,* **29,** 1303–1313.

Le Traon, P. Y., F. Nadal, and N. Ducet, 1998: An improved mapping method of multisatellite altimeter data. *J. Atmos. Oceanic Technol.,* **15,** 522–534.

Liu, Q., S. Wang, Q. Wang, and W. Wang, 2003: On the formation of Subtropical Countercurrent to the west of the Hawaiian Islands. *J. Geophys. Res.,* **108,** 3167, doi:10.1029/2002JC001366.

Nakamura, H., and A. S. Kazmin, 2003: Decadal changes in the North Pacific oceanic frontal zones as revealed in ship and satellite observations. *J. Geophys. Res.,* **108,** 3078, doi:10.1029/1999JC000085.

Niiler, P. P., N. A. Maximenko, G. G. Panteleev, T. Yamagata, and D. B. Olson, 2003: Near-surface dynamical structure of the Kuroshio Extension. *J. Geophys. Res.,* **108,** 3193, doi:10.1029/2002JC001461.

Noh, Y., B. Y. Yim, S. H. You, J. H. Yoon, and B. Qiu, 2007: Seasonal variation of eddy kinetic energy of the North Pacific Subtropical Countercurrent simulated by an eddy-resolving OGCM. *Geophys. Res. Lett.,* **34,** L07601, doi:10.1029/2006GL029130.

Pedlosky, J., 1987: *Geophysical Fluid Dynamics.* 2nd ed. Springer-Verlag, 710 pp.

Press, W. H., S. A. Teukolsky, W. T. Vettering, and B. P. Flannery, 1992: *Numerical Recipes.* Cambridge University Press, 963 pp.

Qiu, B., 1999: Seasonal eddy field modulation of the North Pacific Subtropical Countercurrent: TOPEX/POSEIDON observations and theory. *J. Phys. Oceanogr.,* **29,** 2471–2486.

——, and S. Chen, 2004: Seasonal modulations in the eddy field of the South Pacific Ocean. *J. Phys. Oceanogr.,* **34,** 1515–1527.

——, and ——, 2006: Decadal variability in the formation of the North Pacific Subtropical Mode Water: Oceanic versus atmospheric control. *J. Phys. Oceanogr.,* **36,** 1365–1380.

——, D. Koh, C. Lumpkin, and P. Flament, 1997: Existence and formation mechanism of the North Hawaiian Ridge Current. *J. Phys. Oceanogr.,* **27,** 431–444.

——, N. Schneider, and S. Chen, 2007: Coupled decadal variability in the North Pacific: An observationally constrained idealized model. *J. Climate,* **20,** 3602–3620.

Reynolds, R. W., N. A. Rayner, T. M. Smith, D. C. Stokes, and W. Wang, 2002: An improved in situ and satellite SST analysis for climate. *J. Climate,* **15,** 1609–1625.

Roden, G. I., 1975: On North Pacific temperature, salinity, sound velocity and density fronts and their relation to the wind and energy flux fields. *J. Phys. Oceanogr.,* **5,** 557–571.

Roemmich, D., and J. Gilson, 2001: Eddy transport of heat and thermocline waters in the North Pacific: A key to interannual/decadal climate variability? *J. Phys. Oceanogr.,* **31,** 675–687.

Taguchi, B., S.-P. Xie, N. Schneider, M. Nonaka, H. Sasaki, and Y. Sasai, 2007: Decadal variability of the Kuroshio Extension: Observations and an eddy-resolving model hindcast. *J. Climate,* **20,** 2357–2377.

Takeuchi, K., 1986: Numerical study of the seasonal variations of the Subtropical Front and the Subtropical Countercurrent. *J. Phys. Oceanogr.,* **16,** 919–926.

Wallace, J. M., and D. S. Gutzler, 1981: Teleconnections in the geopotential height field during the Northern Hemisphere winter. *Mon. Wea. Rev.,* **109,** 784–812.

Welander, P., 1981: Mixed layer and fronts in simple ocean circulation model. *J. Phys. Oceanogr.,* **11,** 148–152.

White, W. B., K. Hasunuma, and H. Solomon, 1978: Large-scale seasonal and secular variability of the Subtropical Front in the western North Pacific from 1954 to 1974. *J. Geophys. Res.,* **83,** 4531–4544.

Xie, S.-P., W. T. Liu, Q. Liu, and M. Nonaka, 2001: Far-reaching effects of the Hawaiian Islands on the Pacific ocean-atmosphere system. *Science,* **292,** 2057–2060.

Yamanaka, G., H. Ishizaki, M. Hirabara, and I. Ishikawa, 2008: Decadal variability of the Subtropical Front of the western North Pacific in an eddy-resolving ocean general circulation model. *J. Geophys. Res.,* **113,** C12027, doi:10.1029/2008JC005002.